International Journal of Impact Engineering 186 (2024) 104892

Contents lists available at ScienceDirect

International Journal of Impact Engineering

journal homepage: www.elsevier.com/locate/ijimpeng

Impact dynamics of a free-falling reference test mass in space

D. Vignotto [a,c,*], D. Bortoluzzi [b,c]

[a] Department of Physics, University of Trento, Via Sommarive 14, 38123, Trento, Italy
[b] Department of Industrial Engineering, University of Trento, Via Sommarive 9, 38123, Trento, Italy
[c] Trento Institute of Fundamental Physics and Applications, National Institute for Nuclear Physics (INFN), Via Sommarive 14, 38123, Trento, Italy

ARTICLE INFO

Keywords:
Free-falling objects
Three-dimensional impact
Impact detection
Restitution coefficient
Gold-platinum bodies impact

ABSTRACT

Outer space may constitute a privileged environment for experiments involving impacts. In fact, disturbing phenomena like drag or weight forces are negligible and a nearly pure free-fall state may be achieved for the impacting bodies. The case analysed in this manuscript comes from the initialization of the science phase of a space mission (LISA Pathfinder, flown in 2015), in which an extended metallic body – starting from a caged configuration – was released to free-fall inside a spacecraft by a dedicated mechanism, the grabbing positioning and release mechanism (GPRM). During the release phase, the test mass (TM) experienced some impacts with the GPRM end effector, before being electrostatically controlled to its nominal position, i.e. still in the centre of the hosting electrode housing. The impact dynamics of the TM therefore resulted critical, since it helped reduce its kinetic energy with respect to the spacecraft. In this paper, the TM position and attitude telemetry signals are analysed, and the impacts coefficient of restitution is calculated, providing reference values for similar space instruments, where a free-falling reference body is used (for instance, for geodesy and/or spacecraft navigation).

1. Introduction

In the framework of space technology, impacts constitute a critical issue which has been drawing the attention of relevant research activities. The criticality of impacts first arose concerning the risk of damage produced by meteoroids and space debris, in a range of velocities up to hundreds of $\mathrm{km\,s^{-1}}$. Since the late forties, hyper-velocity impacts (HVI) are studied and strategies to mitigate their effect on the spacecraft are formulated and tested [1]. Particular attention is paid to critical items hosted on board of spacecraft such as pressure vessels [2], solar arrays [3] or thrusters [4], whose failure may lead to a premature end of the mission. The approach, mainly experimental, is organized in terms of parameter space of the impacting body, with scaling formulas which make it possible to transverse the different domains explored by testing facilities [5]. Analytical and numerical models that describe the impact dynamics are introduced and compared with experimental results [6], used to predict the effect of non-testable conditions [7], investigate the effect of the shape and attitude of the impacting body [8] or the fine structure of the impacted system [9].

In general, the models used are kept relatively simple (single degree of freedom) and describe the impact at macro-scale, neglecting many of the mechanisms responsible for the effect of impacts at nano-scale.

A possible limitation in the study of impacts is due to the environment in which experiments are generally performed. On Earth, for example, it is impossible to study a three-dimensional impact without compensating for the gravitational force, and, in general, high relative impact velocities are studied, since friction would largely affect the motion of the colliding bodies in case the collision energy is limited. In this article, the case of impacts of two bodies floating in space is treated, exploiting the in-flight data of a drag-free mission flown in 2015–2017. The mission, called laser interferometer space antenna (LISA) Pathfinder, also referred to as LPF, involves free-falling proof masses in the measurement. The main advantage of studying impacts in the outer space environment is the total absence of weight and drag forces, which are unavoidable on Earth. Moreover, since the two bodies in contact are floating, and their relative position is measured along all six degrees of freedom (DOFs), there are no constraints on the direction of the collision and on its location relative to the bodies geometry. On the contrary, some drawbacks are present relative to the LPF case. In particular, the mission instrumentation was not designed to test impacts. In fact, according to the nominal experiment procedure, impacts should be avoided. For this reason, the LPF sensor was provided with a low frequency control loop on the proof mass position and attitude relative to the spacecraft. As a consequence, the telemetry data are not ideal to perform the analysis of impacts and their processing and the synthesis of results sets a significant challenge.

* Corresponding author at: Department of Physics, University of Trento, Via Sommarive 14, 38123, Trento, Italy.
E-mail address: davide.vignotto@unitn.it (D. Vignotto).

https://doi.org/10.1016/j.ijimpeng.2024.104892
Received 3 October 2023; Received in revised form 24 December 2023; Accepted 11 January 2024
Available online 17 January 2024

In this article, an in-depth analysis of the in-flight data is carried out, with the aim to extract the most information about impacts from the low frequency signals. In Section 2, the LPF mission is briefly described, focussing on the aspect of the unpredicted impacts of the TM with the surrounding elements. In Section 3, the in-flight data are analysed, describing the algorithms developed to extract the desired information. In Section 4 the results returned by the analysis are presented, with a focus on the calculation of the restitution coefficient and the estimation of the unknown location of the impact. Finally, in Section 5, the final conclusions are drawn, underlining the results and the limitations of the calculation carried out, and indicating possible future improvements.

2. LISA pathfinder and the injection into a geodesic of a reference body

The scientific experiment onboard of the LPF spacecraft is based on the drag-free technology, which is used to set into free-fall two 2 kg gold-platinum test masses (TMs) inside dedicated electrode housings (EHs). The TM and the EH are the main components of the gravitational reference sensor (GRS). The goal of the mission was to reach a level of free-fall purity below $3 \times 10^{-14}\,\mathrm{m\,s^{-2}\,Hz^{-1/2}}$ at 1 mHz on the relative acceleration of the two masses. This challenging requirement was achieved with wide margin, paving the way for the gravitational waves measurement from space [10,11].

Each TM, initially locked with respect to the EH, must be released into free fall prior to the initialization of the science phase. The electrode housing has two functions, which are (I) to measure the TM position and attitude by means of capacitive sensing and (II) to apply an electrostatic control force on the TM to keep it in the centre once it has been released. A relevant technological challenge is constituted by the injection of the TM into free-fall, starting from a configuration in which it is hardly constrained for the spacecraft launch phase. In fact, strict requirements are imposed on the TM velocity after the release (below $5\,\mu\mathrm{m\,s^{-1}}$ and $100\,\mu\mathrm{rad\,s^{-1}}$ for the linear and angular components respectively), to guarantee that the limited electrostatic control force is sufficient to capture it in the centre of the EH. At launch, the two masses are caged by a dedicated high pre-load mechanism ($\approx 1 \times 10^3$ N), called caging and vent mechanism (CVM, [12]). Later on, after the in-orbit phase, the masses are handled by a low pre-load mechanism ($\approx$1 N), called grabbing positioning and release mechanism (GPRM, [13]).

The transition from the CVM to the GPRM is performed to reduce the pre-load force on the TM, as well as to engage a dedicated contact area between the TM and the mechanism end effectors, improving the feasibility of a compliant TM release into free-fall.

The GPRM is composed of two nearly identical halves, located on two opposite sides of the TM along z direction (see Fig. 1). Two cylindrical plungers (made of gold-platinum alloy) protrude from the two units towards the centre of the EH, from two opposite sides, firmly grabbing the TM when their heads fit inside dedicated indents present on its z faces. Each plunger is moved back and forth by a NEXLINE piezo-walk linear actuator, and its position is measured by a strain gauge sensor. The head shape of the plunger on the z+ side is conical, while the z− plunger head is pyramidal. In this way, when the TM is grabbed, its rotation about the z-axis (angle φ) is not overconstrained.

Starting from the grabbed TM, its injection into free-fall is performed with a procedure involving different phases. In order to further reduce the contact area and the preload force on the TM, two tips, coaxial to the plungers, are extended from the plunger heads. The tips are extended by a piezo-stack actuator and apply a pre-load force on the bottom of each TM indent, called landing area. Simultaneously with the tip extension, the two plungers are retracted, creating a limited clearance with the TM indent surfaces (approximately 14 μm along z in nominal conditions, see Fig. 1). The transition from the plungers to the tips is called handover.

According to the nominal geometries of the involved components, after the handover the two tips should be the only end-effectors in contact with the TM. In this configuration, the TM is ready to be released into free fall (pre-release phase), and this is done by simultaneously and quickly retracting the two tips. The final step of the release procedure is to retract the two plungers inside the envelope of the EH.

After the release, the electrostatic control force is activated to capture the TM in the centre of the EH, counteracting its initial momentum induced by the release forces arising on the landing areas at the tips retraction.

According to several pre-mission studies, in the nominal configuration the GPRM should guarantee a successful release (i.e., a TM release velocity compliant with the requirements) in >96% of the cases [14]. Unfortunately, during the first mission releases, the GPRM produced an unexpected TM state. Even if the direction of the retraction of the tips is aligned with the z-axis, all the linear and rotational velocity components of the TM were produced. Given the unexpected dynamics of the firsts releases, the following releases were performed relying on impacts between the plungers and the TM, in order to reduce progressively its momentum to a point where it was captured by commanding manually the electrostatic control force. During the extended mission phase (summer 2017), a dedicated campaign of release tests was conducted on the GPRM. The main suspect was that a reduced plunger-TM clearance (assembly misalignment, machining tolerances etc.) produced contacts and subsequent impulses. As a consequence, several modifications to the nominal release procedure were applied, with the main goal of maximizing the TM-plunger clearance in the pre-release phase. In the end, no optimal injection strategy that systematically worked for both GPRMs on board of LPF was found; nevertheless, from the analysis of the test data it was concluded that the unexpected TM state was produced by impacts between the TM and the plunger head, which oscillates at the retraction of the tip [15–17].

After the release, the non compliant initial velocity of the TM produced uncontrollable states, leading to several undesired impacts of the TM with the plunger heads and/or the surrounding EH walls. The electrostatic control force was able to capture the TM, most of the times, only when its kinetic energy was sufficiently reduced by the impacts. The in-flight experiments realized to test the release phase and the GPRM performance yield valuable information also about the impact dynamics of an extended body in a nearly perfect free-fall state. In this work, the in-flight data collected during the extended mission release tests are analysed, focusing on the time intervals where the TM was free falling (i.e., after the release and before the actuation of the electrostatic control force) and studying the effects of the impacts on its motion (Fig. 2).

3. Detection of impacts of the proof mass

The in-flight releases analysed in this work are 216 (108 for each TM) and have been performed in June/July 2017 during the extended mission phase. The analysis presented makes extensive use of the GRS capacitive position sensing data [18,19] from the GRS front-end electronics (FEE), from which the 6 degrees of freedom of the TM (position and attitude, sampled at 10 Hz) are estimated. Additionally, the GPRM telemetry (sampled at 1 Hz) is used to retrieve (I) the commanded tip positions, useful to identify the release instant with 1 s accuracy, and (II) the measured plunger positions.

It should be noted that, in the extended mission releases analysed, the FEE is in its “wide-range” mode, where relatively large displacements are expected and the electrostatic actuation forces are larger if compared to the science phase. Indeed, in the science phase the TM is free-falling and the FEE employs a “high resolution” mode whose sensing and actuation performance have been described in [20,21].

During the TM release a 100 kHz sensing injection voltage is applied both to the GRS injection electrodes and to the GPRM plungers, allowing continuous measurement of the TM position both with the TM mechanically grabbed and with the TM electrically “floating” immediately following the release.

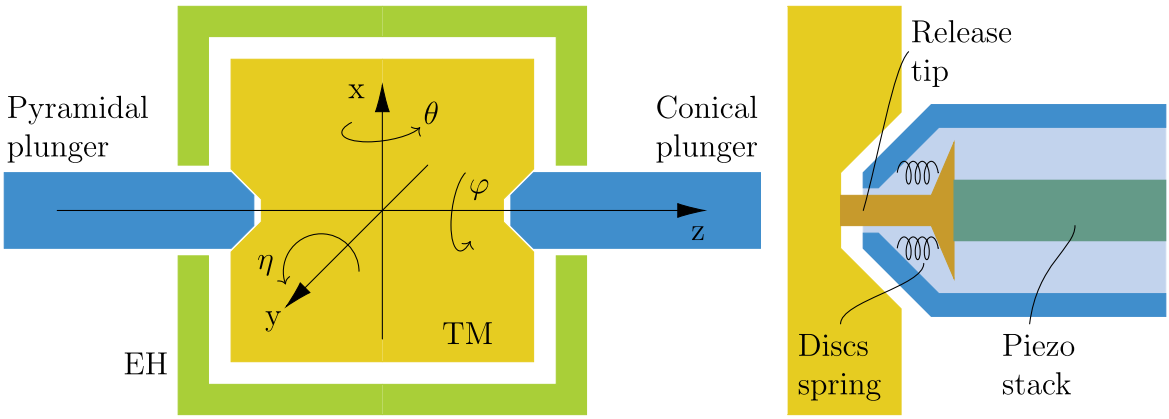

Fig. 1. On the left, sketch showing the GPRM configuration when grabbing TM, and the reference frame expressing the TM position and attitude. The two plungers are in contact with the TM indent surfaces, and their axes are coincident with the z axis. On the right, detail of a single half of the mechanism after the handover to the tips is performed. The TM-plunger clearance along z is limited to 14 µm.

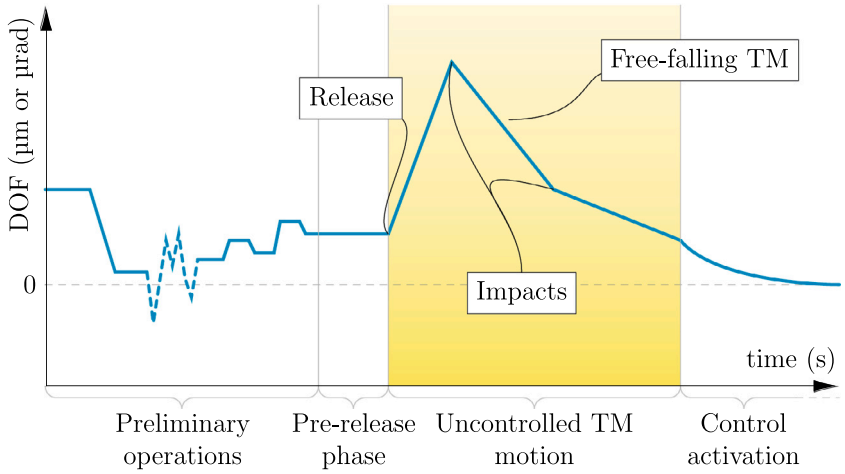

Fig. 2. Schematic graph of the different phases of the injection procedure. The interval of interest in this work is highlighted in yellow. It corresponds to the time interval where the TM is free-falling, eventually impacting with the surroundings, and its motion is not affected by the electrostatic control force.

The goal of the following analysis is to develop an algorithm that (I) finds when the TM is released and (II) detects the impacts the TM undergoes once released. Before developing the algorithm, the noises affecting the TM position/attitude signals before and after the release are characterized. In principle, those noises could be different, since they are related to two different configurations of the GRS. Before the release, the TM is physically connected to the tips/plungers while after the release there are no physical contacts.

The focus is on the tests where there is a large time interval (≥10 s, i.e., at least 100 sampling points) with a still TM before and/or after the release.

The comparison of the pre-release and post-release noises is summarized in Fig. 3, where the amplitude spectral densities are plotted for the six DOFs. Running a χ^2-test [22] on the noise data confirmed the pre-release and post-release noises distribution may be assumed identical. Considering the spectral densities, we also assume that the noise is uncorrelated for any DOF except for z, where a predominant peak is present at the frequency of 1 Hz. For this reason, the analysis of the impacts that the TM underwent after its release is carried out taking into account the different correlation of the noise affecting the TM DOFs, namely considering a white noise for all DOFs except for z Fig. 4.

Moreover, analysing the standard deviation of the noise affecting the signals before and after the release it resulted comparable for both the TMs. The values of the noise standard deviations of the two TMs relative to each DOF are summarized in Table 1. The characterization of the noise makes it possible to develop and predict the statistical performance of an algorithm that searches for impacts on the TM after its release. Such an algorithm is divided in two parts, which are described in the following Sections and reported in Appendix A.

Table 1
Average noise standard deviations σ_s affecting the in-flight telemetry data for the two TMs.

Param.	x (µm)	y (µm)	z (µm)	θ (µrad)	η (µrad)	φ (µrad)
σ_s TM$_1$	0.01	0.01	0.02	0.6	0.8	0.7
σ_s TM$_2$	0.01	0.01	0.02	0.5	0.9	0.7

3.1. Detection of the test-mass release instant

The first part of the algorithm is developed to reliably identify the instant of incipient motion of the TM, i.e., its release, taking into account the presence of the measurement noise. In fact, the proposed criterion defines the TM release when the measurement signal of at least one DOF violates with some persistence the noise statistics.

Given a generic in-flight signal s, a time interval of 5 s ($n_m = 10 \cdot 5 = 50$ data-points) is identified just before the TM release. Such a pre-release time interval, where the TM is still, is identified from the GRS housekeeping telemetry (tip and plunger position signals) and is common to all the six DOFs.

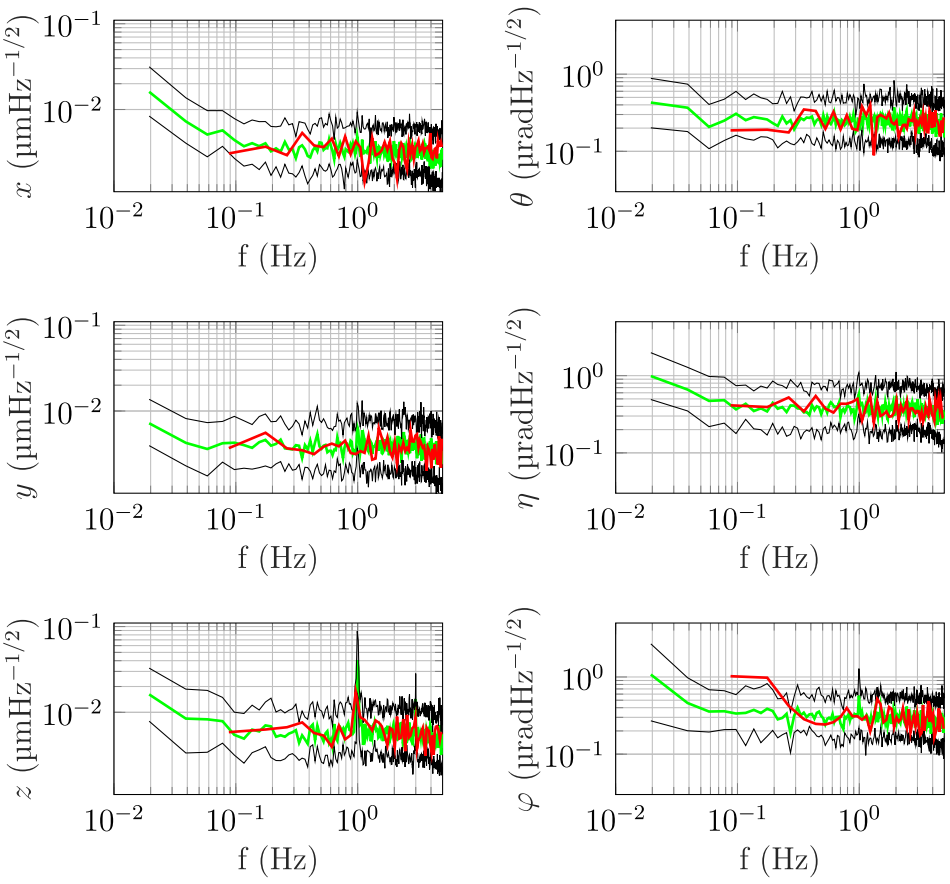

Fig. 3. Amplitude spectral density (ASD) of the noise affecting the six DOFs of the TMs based on large (≥10 s) time intervals where velocity is approximately zero. On each plot, the green line represents the mean ASD of the pre-release noise, and the black lines the ±1 standard deviation. The red line represents the mean ASD of the post-release noise (no standard deviation is shown due to the fact that only three post-release intervals with a still TM were found). The compatibility between the green and red lines suggests that the noise can be assumed stationary across pre-release and post-release phases.

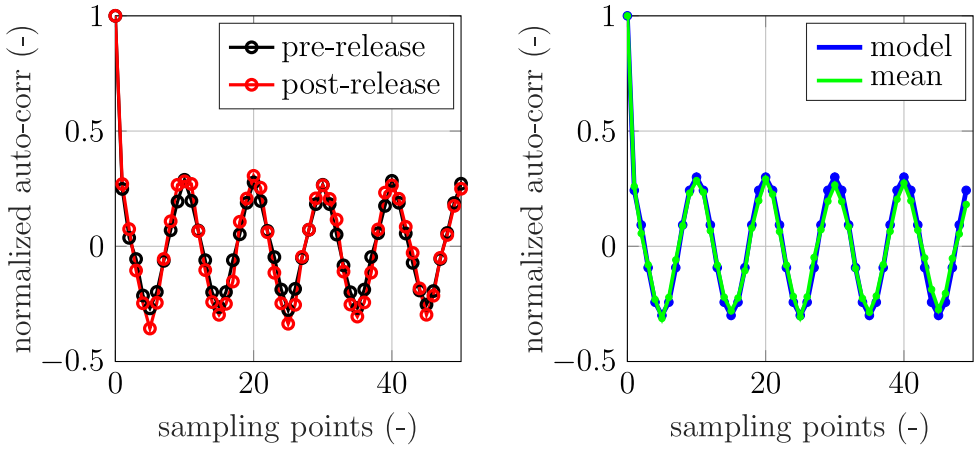

Fig. 4. On the left, auto-correlation function of the z DOF signal in the pre-release (black) and post-release (red) intervals considered for the noise analysis. On the right, comparison between the average auto-correlation function between pre and post release noises (green) and the modelled one (blue).

The sampled points composing the pre-release interval are averaged and the obtained mean value is subtracted from the signal s. Given the large number of points on which the average is performed, its subtraction introduces an uncertainty, expressed in Eq. (1), which is negligible.

$$\sigma_{\text{tot}} = \sqrt{\sigma_s^2 + \sigma_m^2} = \sqrt{\sigma_s^2 + \left(\frac{\sigma_s}{\sqrt{n_m}}\right)^2} \approx 1.01\sigma_s \approx \sigma_s \tag{1}$$

With σ_s the noise standard deviation of the signal s and n_m the number of points of the pre-release interval.

After subtracting the average pre-release value, a moving window, that starts form the last point of the pre-release interval, is considered. The amplitude of the moving window, in terms of the number of points included, is set by the user-defined parameter n_{p}.

The proposed algorithm searches for a set of n_{p} points all exceeding the threshold of $+\kappa\sigma_s$ or $-\kappa\sigma_s$, with κ a user defined parameter.

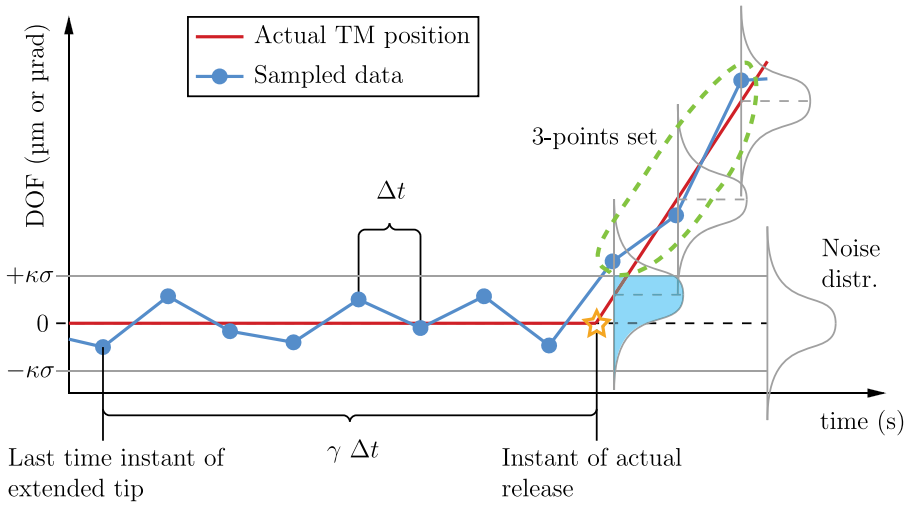

Fig. 5. Scheme illustrating the quantities involved in the detection of the TM release. A single DOF is depicted. The grey curves indicate the noise distributions (normal, with standard deviation σ), that are equal for each sampling point. The shaded areas corresponds to the probability that a sampling point falls inside the $\pm\kappa\sigma$ interval.

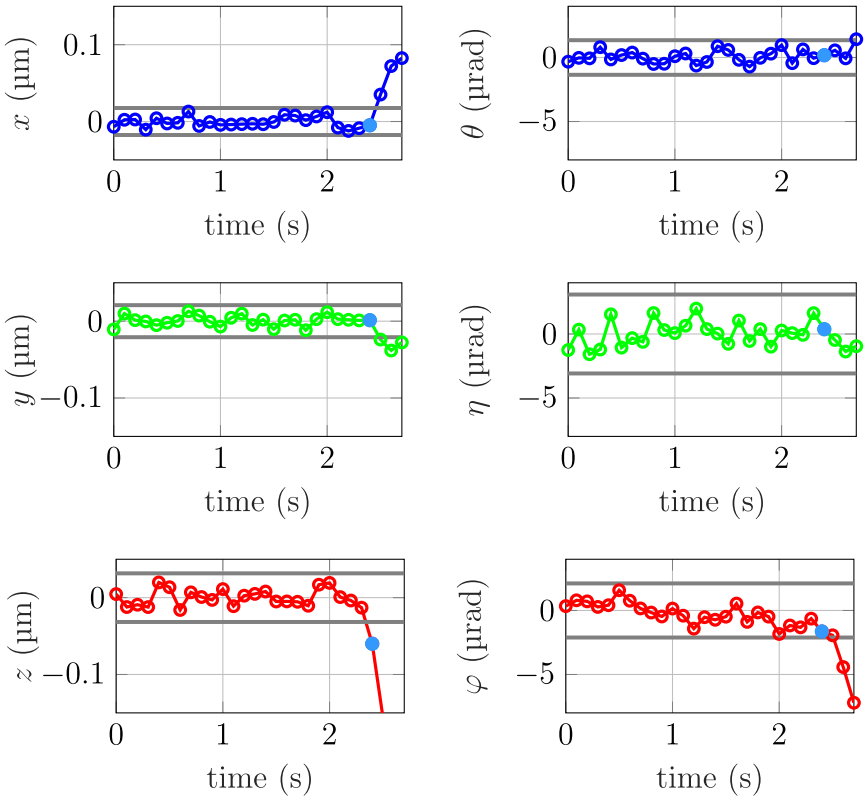

Fig. 6. Six DOFs of the TM_1 for one of the in-flight tests. The pre-release interval (black data points), the mean (dashed line) and the $\pm 3\sigma_s$ interval (solid lines) are shown. The light-blue point corresponds to the estimated release instant.

A scheme showing the algorithm principle is represented in Fig. 5. When a set satisfying the criterion is found, the algorithm stops and returns the time instant corresponding to the first sampling point of the set. Thus, when the algorithm is executed for all the six DOFs of a test, a maximum of six different time instants are found. The final release instant is simply defined as the minimum time instant of the set, in the hypothesis that the incipient TM motion in any of the DOFs corresponds to its actual release. An example of the application of the algorithm to an in-flight test, with the resulting release instant, is depicted in Fig. 6.

3.1.1. Release detection algorithm statistical performance

In this Section, the performance of the first part of the algorithm is addressed from a statistical point of view. The hypotheses formulated on a generic time window of n_p points are the following:

- H_0: the TM velocity is null (no release)
- H_1: the TM velocity is not null (release)

From now on, the probability of a type I error (H_0 rejected when true) is defined as α and the probability of a type II error (H_1 rejected when true) is defined as β

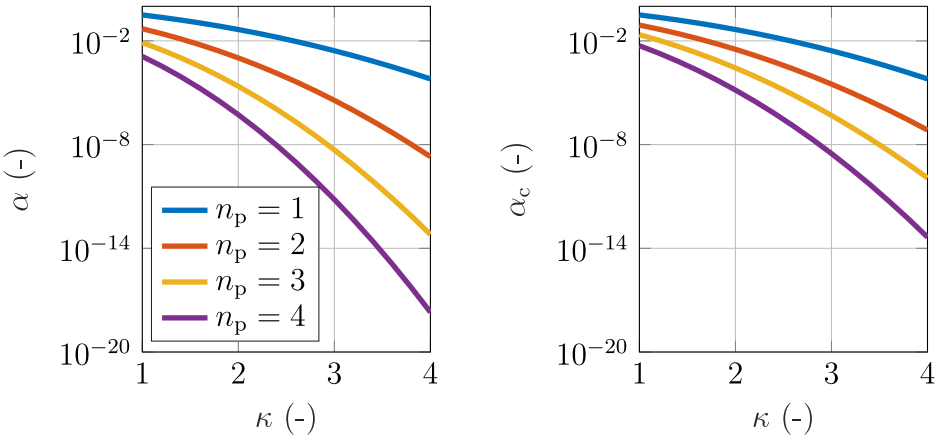

Fig. 7. Type I error probability α of detecting a TM release. Both the uncorrelated case (left) and correlated case (right) are shown.

3.1.1.1. Case of uncorrelated noise. When the signal s has an uncorrelated noise, the probability α, i.e., that all the n_p samples of the time window are larger than $+\kappa\sigma_s$ or smaller than $-\kappa\sigma_s$, may be calculated as shown in Eq. (2).

$$\alpha = 2\left(1 - \frac{1}{2}\mathrm{erfc}\left(-\frac{\kappa}{\sqrt{2}}\right)\right)^{n_p} \tag{2}$$

where erfc() is the complementary normal error function, defined as $\mathrm{erfc}(x) = 1 - \mathrm{erf}(x)$.

As clearly shown in Fig. 7, increasing n_p reduces the risk of a false detection of the release event, however, it also reduces the sensitivity of the algorithm (addressed below) and increases the risk of including in the time window following events like post-release impacts. For the same uncorrelated noise signal s, the probability β, i.e., missing the detection of a release, is computed in the following. In this case, an intermediate step is necessary, since the exact release instant is not known a priori. Firstly, the probability β_γ is computed as shown in Eq. (3).

$$\begin{aligned}\beta_\gamma = 1 &- \prod_{n=1}^{n_p}\left(1 - \frac{1}{2}\mathrm{erfc}\left(\frac{\nu(\gamma+n-1)-\kappa}{\sqrt{2}}\right)\right) \\ &- \prod_{n=1}^{n_p}\left(\frac{1}{2}\mathrm{erfc}\left(\frac{\nu(\gamma+n-1)+\kappa}{\sqrt{2}}\right)\right)\end{aligned} \tag{3}$$

where γ identifies the time lead (divided by the sampling time) of the actual release instant with respect to the sampled point identified by $n = 1$, while $\nu = v\Delta t/\sigma_s$ is the release velocity v re-scaled with respect to the reference velocity given by the ratio between the noise standard deviation σ_s and the sampling interval Δt. The uncertainty of the release instant with respect to the first point, $n = 1$, is ruled by the sampling frequency (1 Hz) of the GPRM housekeeping data, including the release tip and the plunger positions. This means that the maximum time lead γ of the actual release with respect to the first identified point of released TM may be equal to 10 sampling intervals at most. Since there is no further information about the actual release, the probability density function of γ is supposed uniform, therefore the β_γ probability of Eq. (3) is simply averaged in the γ domain $\{0, \gamma_{max}\}$ to finally compute β, as shown in Eq. (4).

$$\beta = \frac{1}{\gamma_{max}}\int_0^{\gamma_{max}} \beta_\gamma \, \mathrm{d}\gamma \tag{4}$$

As shown in Fig. 8, larger release velocities (i.e., larger ν) produce a small risk of missed detection, whereas increasing the threshold κ reduces the sensitivity of the detection algorithm enhancing the probability β. The plot also shows that reasonable values for the window length n_p (i.e., below 10) produce a negligible influence on the sensitivity. As a consequence, in the present case of study the choice of n_p is based on the requirement to limit the risk of false detection and of including post-release events

3.1.1.2. Case of correlated noise. To analyse the case of correlated noise, the signal s is considered having a normalized auto-correlation function $R_{ss}(\tau)$. Such a function, represented in Eq. (5) is modelled as a sinusoidal discrete function, which resembles the one observed in the flight data for the z DOF (Fig. 4).

$$R_{ss}(\tau) = \begin{cases} 1 & \tau = 0 \\ A\cos\left(\frac{f}{2\pi}\tau\right) & \tau > 0 \end{cases} \tag{5}$$

where the frequency f, equal to 1 Hz, and the normalized amplitude A, equal to 0.3, are estimated by fitting the model of $R_{ss}(\tau)$ to the in-flight data auto-correlation.

In this case, to compute the probabilities α_c and β_c (subscript c indicates the noise is correlated) it is necessary to consider a multivariate normal distribution with covariance matrix derived form the auto-correlation of the noise. The covariance matrix, called $\boldsymbol{\Sigma}$, is derived from the Toeplitz matrix of the autocorrelation, as shown in Eq. (6).

$$\boldsymbol{\Sigma} = \mathrm{Toep}(\mathbf{R}_{ss}(\tau)) = \begin{bmatrix} 1 & \rho_{12} & \cdots & \rho_{1n_p} \\ \rho_{12} & 1 & \cdots & \rho_{2n_p} \\ \vdots & \vdots & \ddots & \vdots \\ \rho_{1n_p} & \rho_{2n_p} & \cdots & 1 \end{bmatrix} \tag{6}$$

The α_c probability, plotted in Fig. 7, is equal to:

$$\alpha_c = 2\,\mathrm{CDF}(\mathcal{N}_{n_p}(\mathbf{0}, \boldsymbol{\Sigma}), -\kappa\mathbf{1}) \tag{7}$$

where CDF() is the cumulative density function, $\mathcal{N}_{n_p}()$ is the n_p-dimensional multivariate normal distribution, $\mathbf{0}$ is a $n_p \times 1$ null array, $\boldsymbol{\Sigma}$ is the $n_p \times n_p$ covariance matrix of the noise, and $-\kappa\mathbf{1}$ is a $n_p \times 1$ array with entries equal to $-\kappa$.

The β_c probability in the case of correlated noise involves an intermediate step, exactly as shown for the correlated case. Adopting the same notation defined above, the $\beta_{c,\gamma}$ probability is equal to:

$$\beta_{c,\gamma} = 1 - \mathrm{CDF}(\mathcal{N}_{n_p}(\boldsymbol{\mu}(\gamma), \boldsymbol{\Sigma}), -\kappa\mathbf{1}) - \mathrm{CDF}(\mathcal{N}_{n_p}(\boldsymbol{\mu}(\gamma), \boldsymbol{\Sigma}), 2\boldsymbol{\mu} - \kappa\mathbf{1}) \tag{8}$$

where $\boldsymbol{\mu}(\gamma)$ is a $n_p \times 1$ array containing the mean values of n_p consecutive points of the signal s that follow the release instant. Thus, the array $\boldsymbol{\mu}(\gamma)$ can be expressed as:

$$\boldsymbol{\mu}(\gamma) = v\Delta t\,\{\gamma, \gamma+1, \gamma+2, \ldots, \gamma+n_p-1\} \tag{9}$$

where v is the release velocity of the TM, Δt is the sampling time and γ identifies the time lead (divided by the sampling time) of the actual release instant. Since the release instant is unknown, the β_c probability, plotted in Fig. 9, is computed integrating $\beta_{c,\gamma}$ on the domain $\{0, \gamma_{max}\}$, introducing the same hypothesis of the uncorrelated case (Eq. (10)).

$$\beta_c = \frac{1}{\gamma_{max}}\int_0^{\gamma_{max}} \beta_{c,\gamma} \, \mathrm{d}\gamma \tag{10}$$

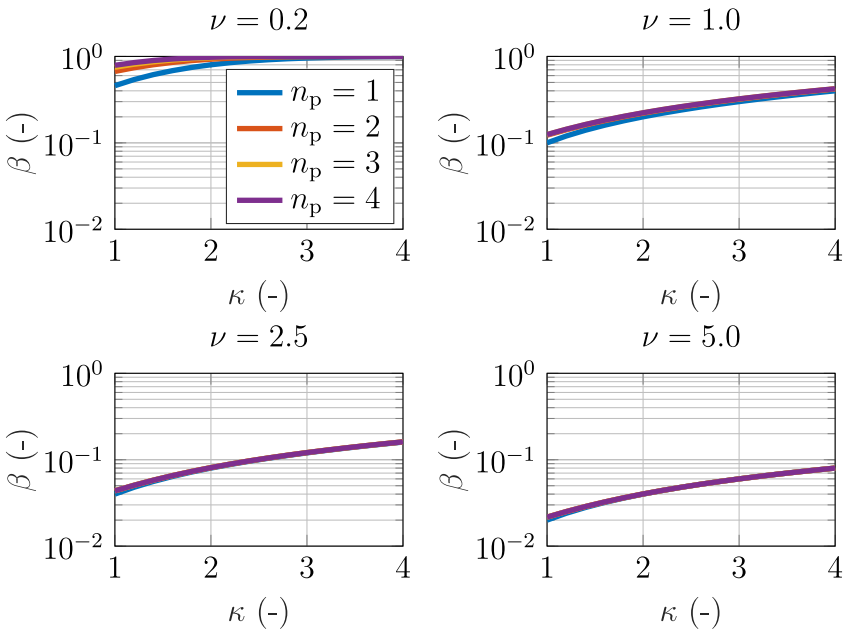

Fig. 8. Type II error probability β of detecting a TM release for an uncorrelated signal. Probability is plotted for different values of ν.

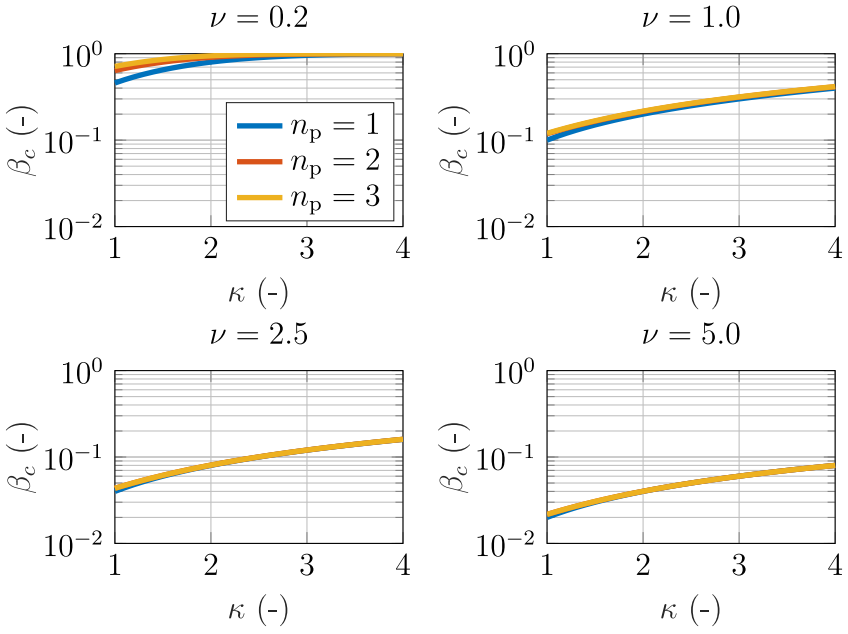

Fig. 9. Type II error probability β_c of detecting a TM release for a correlated signal. Probability is plotted for different values of ν.

Table 2
Values of the parameters involved in the computation of the α and β probabilities for the detection of the release instant. The values are computed from the analysis of the in-flight data.

Parameters	Value	Unit
Δt	0.1	s
γ_{max}	10.0	(–)
ρ_{12}	0.024	(–)
ρ_{13}	0.009	(–)

3.1.2. Numerical evaluation of release instant detection probabilities

To detect the release instant of the in-flight tests, the user-defined parameters n_p and κ are both set equal to 3. The other algorithm parameters are estimated from the noise analysis of the in-flight data. Some of them are independent of the specific DOF and are reported in Table 2, while the standard deviation σ_s depends both on the DOF and the TM (Table 1). Moreover, the type II probability depends also on the actual release velocity of the TM. As an example, in Table 3 the probabilities α and β of the TM_1 DOFs are represented, considering two cases for the TM velocity (TM_2 has similar values). Observing the probabilities reported in the table, it should be noticed that the values

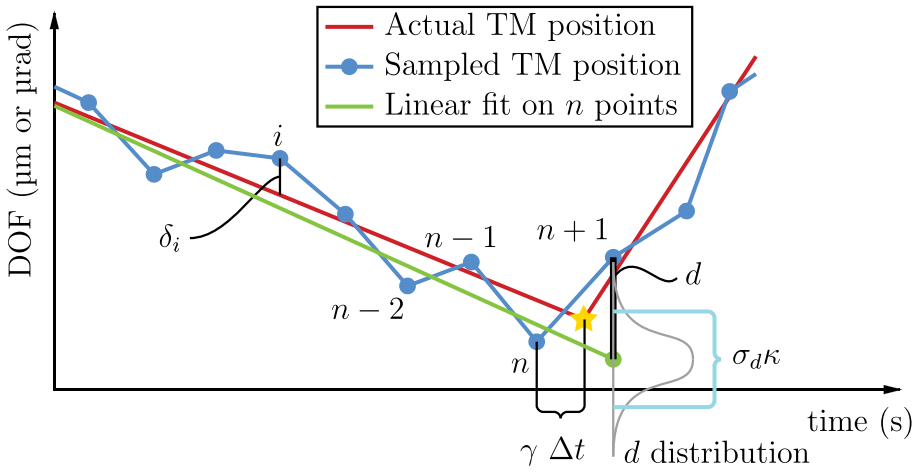

Fig. 10. Scheme illustrating the quantities involved in the computation of the α and β probabilities for the detection of impact on the free-falling TM. A single DOF is depicted. The distribution relative to the $n+1$-th point (normal, with standard deviation σ_d) is shown.

Table 3
Type I and type II probabilities of the release instant detection algorithm for the TM_1 DOFs. The type II probability is evaluated for two different TM velocities. Left column: velocity equal to one fifth of the requirement. Right column: velocity equal to the requirement.

DOF	α	β for $v = v_{req}/5$	β for $v = v_{req}$
x	4.92×10^{-9}	3.00×10^{-2}	0.60×10^{-2}
y	4.92×10^{-9}	3.00×10^{-2}	0.60×10^{-2}
θ	4.92×10^{-9}	7.50×10^{-2}	1.50×10^{-2}
η	4.92×10^{-9}	12.09×10^{-2}	2.40×10^{-2}
φ	4.92×10^{-9}	10.54×10^{-2}	2.10×10^{-2}
	α_c	β_c for $v = v_{req}/5$	β_c for $v = v_{req}$
z	6.36×10^{-7}	6.00×10^{-2}	1.20×10^{-2}

of the parameters κ and n_p used in the analysis derive from the trade off between having a very low probability of detecting a false release (α probability) while maintaining a sufficiently low probability of missing an actual release (β probability) with a significant residual velocity.

3.2. Detection of test-mass post-release impacts

After the release instant is estimated in the first part of the algorithm, the impacts the TM undergoes after the release event are detected in the second part, which is based on the linear regression. *The idea is to apply a linear regression to the position and attitude TM signals in a moving time frame to find the time intervals where the TM has a constant velocity*.

A scheme showing the algorithm principle is represented in Fig. 10. The hypothesis behind this choice is that the trend the signals should follow after the release is a straight line consistent with the noise statistics, and so that any deviation from the linear trajectory is caused by an impact.

The base case is to consider a set of n points taken from a given DOF s, generated by a constant velocity TM motion. The ith point of the set is then expressed as shown in Eq. (11), where v is the actual velocity of the TM, Δt the sampling time and δ_i the measurement noise at the ith sampling time.

$$s_i = t_i\, v + \delta_i = i\Delta t\, v + \delta_i \tag{11}$$

The measurement noise δ_i is extracted from a zero-mean Gaussian distribution with standard deviation σ_s.

The next steps of the sub-algorithm are to apply a linear fit to the n points and then to evaluate the distance d between the fit line and the point following the initial set ($n+1$-th point). It is then checked if the distance d is below or above a user-defined threshold. This procedure is repeated for all the six DOFs of the TM. If for all DOFs the distance d is below the threshold, the $n+1$-th point is considered not to violate the noise statistics in the hypothesis of constant TM velocity. Thus, the point is added to the initial set of n points and the next algorithm iteration starts from the updated initial set. If even in a single DOF the distance d is above the threshold, the $n+1$-th point is considered generated from an impact. In this case, the initial interval of n points cannot be extended and is saved. The next iteration of the sub-algorithm will start from an initial set composed of the two points $n+1$-th and $n+2$-th. Going more in detail, the calculation of the threshold for the distance d depends on the noise correlation. In case the noise is uncorrelated, the distance d is computed thanks to a standard linear fit, and its closed form expression is shown in Eq. (12).

$$d = \frac{\sum_{i=1}^{n} \delta_i\,(6i - 2(n+2)) - (n-1)n\delta_{n+1}}{(n-1)n} \tag{12}$$

Since d is a linear combination of the noise realizations δ_i, the probability distribution of d is Gaussian, with the standard deviation shown in Eq. (13).

$$\sigma_d = \sqrt{\sigma_s^2\left(\sum_{i=1}^{n}\left(\frac{6i-2(n+2)}{(n-1)n}\right)^2 + 1\right)} = \sigma_s\sqrt{\frac{(1+n)(2+n)}{(n-1)n}} \tag{13}$$

where σ_s is the standard deviation of the noise.

The threshold to determine if d is acceptable or not, called t_d, is computed setting a desired value for the type I probability α, i.e, the probability that d is outside the interval $\pm t_d$ (Eq. (14)).

$$t_d = \kappa\sigma_d = \underbrace{\sqrt{2}\mathrm{erfc}^{-1}(\alpha)}_{\kappa}\ \underbrace{\sigma_s\sqrt{\frac{(1+n)(2+n)}{(n-1)n}}}_{\sigma_d} \tag{14}$$

where α is now a user-defined parameter of the sub-algorithm. When the noise is correlated, the first difference with the previous case is that the linear fit parameters are weighted by the covariance matrix of the noise [23], as shown in Eq. (15).

$$\mathbf{p} = \left(\mathbf{T}^\top\boldsymbol{\Sigma}^{-1}\mathbf{T}\right)^{-1}\mathbf{T}^\top\boldsymbol{\Sigma}^{-1}\,\mathbf{s} \tag{15}$$

where $\mathbf{p}$ and $\mathbf{s}$ are the column vectors of the fit parameters and the data sampled points respectively. The matrices $\boldsymbol{\Sigma}$ and $\mathbf{T}$ are the noise covariance matrix and the design matrix respectively (superscripts $\top$ and -1 indicate transpose and inverse operators).

In this case, the expression of d results different, thus, also the distribution of d is different. Conveniently, it is still linear with respect to the noise realizations δ_i, so the only difference with the uncorrelated case is the value of the standard deviation σ_d.

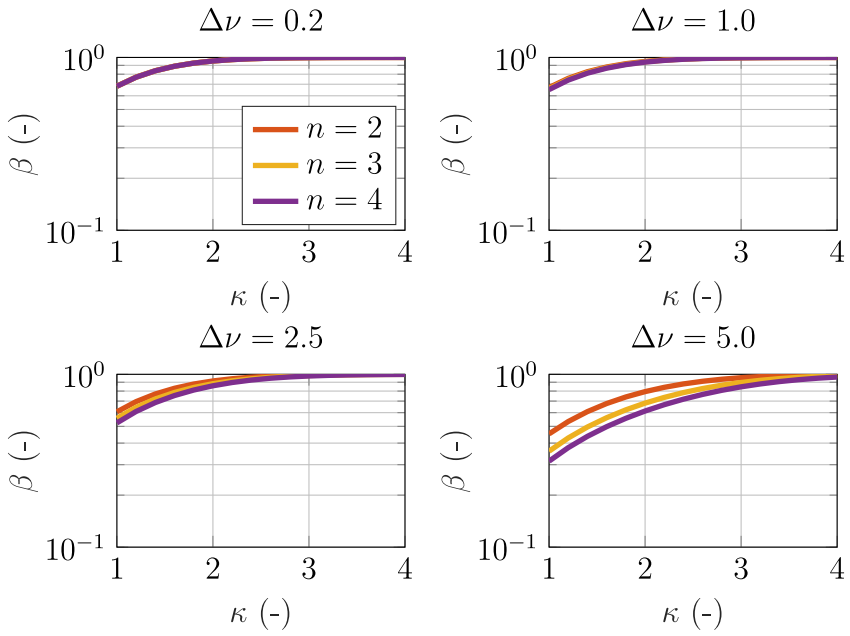

Fig. 11. Type II error probability β of detecting an impact on the free-falling TM for an uncorrelated noise signal. The probability is plotted for different values of $\Delta\nu$.

Since in this case there is no closed form for d, the values of the coefficients c_i that multiply the noise realizations δ_i are computed numerically for different values of n. Using those coefficients, it is possible to compute the threshold t_d for the correlated case as shown in Eq. (16).

$$t_d = \kappa\sigma_d = \underbrace{\sqrt{2}\mathrm{erfc}^{-1}(\alpha)}_{\kappa}\ \underbrace{\sqrt{\mathbf{c}^\top \boldsymbol{\Sigma}\,\mathbf{c}}}_{\sigma_d} \tag{16}$$

where α is the same user-defined parameter of the uncorrelated noise case, $\mathbf{c}$ is the $n\times 1$ array of the coefficients c_i, and $\boldsymbol{\Sigma}$ is the $n\times n$ covariance matrix of the noise (defined in Eq. (6))

3.2.1. Impact detection algorithm statistical performance

Similarly to what was done in Section 3.1.1, the type I and type II error probabilities are evaluated to estimate the algorithm performance from a statistical point of view.

As previously stated, the type I probability α is a user-defined parameter of this sub-algorithm, and is the same for both the correlated and uncorrelated noise cases. It expresses the probability that the $n+1$-th point is considered generated by an impact when in fact it is not.

Instead, the β probability, i.e., the probability of not considering the $n+1$-th point as a consequence of an impact while in fact it is, needs to be evaluated, and some distinctions between the uncorrelated and correlated noise cases are necessary.

To evaluate the β probability, the $n+1$-th point should be expressed as it was generated by an impact taking place between the nth and the $n+1$-th points. Such an expression is shown in Eq. (17).

$$s_{n+1} = \Delta t(n+\gamma)\,v_1 + \Delta t(1-\gamma)\,v_2 + \delta_{n+1} \tag{17}$$

where the impact took place at the time instant $(n+\gamma)\,\Delta t$ with unknown $\gamma \in \{0,1\}$. The quantities v_1 and v_2 represent the TM velocity before and after the impact respectively, expressed in the GRS reference frame and considered with their sign.

3.2.1.1. Case of uncorrelated noise. Considering the uncorrelated noise case, the distance d between the point s_{n+1} and the linear fit based on the previous n points is expressed in Eq. (18).

$$d = \frac{\sum_{i=1}^{n}\delta_i\,(6i-2(n+2)) - (n-1)n\delta_{n+1}}{(n-1)n} + (\gamma-1)\Delta t\Delta v \tag{18}$$

where Δv is defined as $v_2 - v_1$. This equation is similar to Eq. (12), apart from the presence of the additional term $(\gamma-1)\Delta t\Delta v$. The standard deviation σ_d in this case is equal to the one computed in Eq. (13), because the additional term is composed of constant quantities.

Adopting the same threshold t_d defined in Eq. (14), and defining $\Delta\nu = \Delta v\Delta t/\sigma_s$, the resulting β_γ probability is shown in Eq. (19).

$$\beta_\gamma = \frac{1}{2}\mathrm{erf}\left(\frac{(\gamma-1)\Delta\nu}{\sqrt{2}\sqrt{\frac{(n+1)(n+2)}{(n-1)n}}} + \frac{\kappa}{\sqrt{2}}\right) - \frac{1}{2}\mathrm{erf}\left(\frac{(\gamma-1)\Delta\nu}{\sqrt{2}\sqrt{\frac{(n+1)(n+2)}{(n-1)n}}} - \frac{\kappa}{\sqrt{2}}\right) \tag{19}$$

Since the value of γ is not known a priori, the average β probability is computed by integrating Eq. (19) in the domain $\{0,1\}$, which corresponds to one sampling interval.

$$\beta = \int_0^1 \beta_\gamma\,\mathrm{d}\gamma \tag{20}$$

The plot of β probability of the detection of impacts in an uncorrelated noise signal are reported in Fig. 11.

3.2.1.2. Case of correlated noise. In the case the noise is correlated, the probability $\beta_{c,\gamma}$ is computed as shown in Eq. (21), where $\sigma_d = \sigma_s\sqrt{\mathbf{c}^\top\boldsymbol{\Sigma}\,\mathbf{c}}$.

$$\beta_{c,\gamma} = \frac{1}{2}\mathrm{erfc}\left(\frac{(\gamma-1)\Delta\nu\sigma_s}{\sqrt{2}\sigma_d} + \frac{\kappa}{\sqrt{2}}\right) - \frac{1}{2}\mathrm{erfc}\left(\frac{(\gamma-1)\Delta\nu\sigma_s}{\sqrt{2}\sigma_d} - \frac{\kappa}{\sqrt{2}}\right) \tag{21}$$

Finally, the probability β_c is computed integrating $\beta_{c,\gamma}$, exactly as in the previous case (Eq. (20) and Fig. 12). The difference from the uncorrelated case is marginal.

3.2.2. Numerical evaluation of impact detection probabilities

When applying the sub-algorithm to the in-flight data, the user-defined parameter α, which directly expresses the type I probability, was set equal to 0.05. Thus, approximately 5% of the times the algorithm discards a point that instead should be added to the previous interval. The probability β strongly depends on $\Delta\nu$ and on the number of points in the interval n. Of course, it is more probable to detect an impact when it produces a large variation of the TM velocity and the interval has a greater number of points. In Table 4 the values of α and β probabilities are reported, considering an interval of $n = 4$ points and for two different values of Δv.

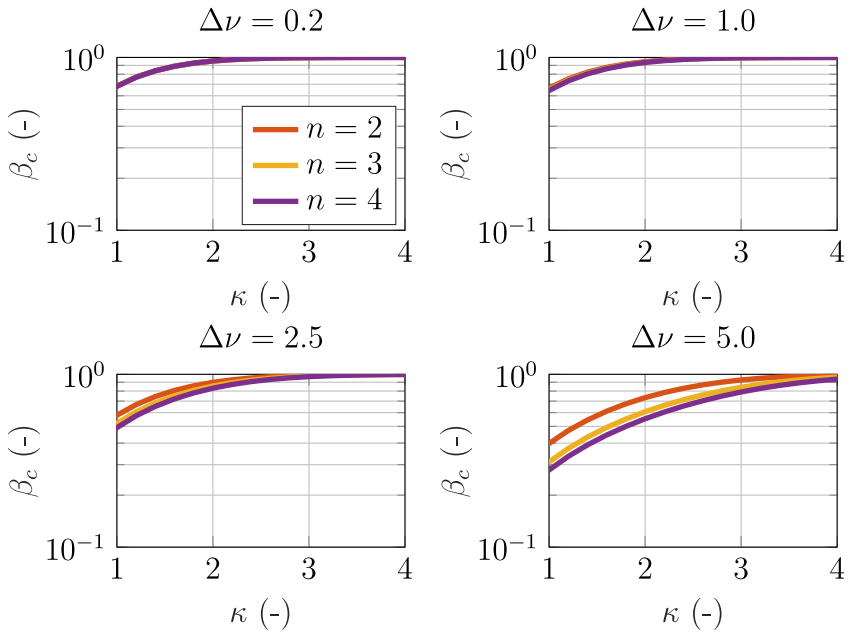

Fig. 12. Type II error probability β_c of detecting an impact on the free-falling TM for a correlated noise signal. The probability is plotted for different values of Δv.

Table 4
Type I and type II probabilities of the impacts detection algorithm for the TM_1 DOFs. Values are computed for number of points $n = 4$. The type I probability α is a user defined parameter, equal to 0.05. The type II probability β (and β_c) is evaluated for two different TM velocities. Left column: delta velocity equal to one fifth of the requirement. Right column: delta velocity equal to the requirement.

DOF	α	β for $\Delta v = v_{req}/5$	β for $\Delta = v_{req}$
x	0.05	0.31	0.06
y	0.05	0.31	0.06
θ	0.05	0.77	0.19
η	0.05	0.85	0.25
φ	0.05	0.82	0.22
	α_c	β_c for $\Delta = v_{req}/5$	β_c for $\Delta = v_{req}$
z	0.05	0.54	0.11

4. Analysis of the in-flight detected impacts

The results of the application of the analysis process described in Section 3 to the flight data are discussed in the following.

The application of the first part of the algorithm allows us to estimate the release instant of the TM on each of the flight test (108 for each TM). Due to the extremely low α probability of false release detection and the low β probability of missing a release with significant TM velocity (greater than the requirements), no particular problem was encountered running the algorithm.

The application of the second part of the algorithm allows us to find the constant velocity intervals, i.e. the time intervals where the TM maintains a constant linear and angular momentum.

In the hypothesis that either a single impact or multiple impacts were responsible for the variation of the TM momentum between two constant velocity intervals, then such event can be characterized estimating the TM velocities before and after the event. Considering the ith event of a test, for a given DOF s, the TM velocities before and after the event are called $v_{s,i}$ and $v_{s,i+1}$ respectively (or $\omega_{s,i}$ in case s is an angular DOF).

Each velocity, along with its uncertainty, is estimated with a linear fit applied to the data points belonging to the considered constant-velocity time interval.

After estimating $v_{s,i}$ and $v_{s,i+1}$ (with their uncertainties) for the six DOFs of the TM, the following quantities are computed:

- $K_i = 1/2 m_{TM}(v_{x,i}^2 + v_{y,i}^2 + v_{z,i}^2) + 1/2(I_{xx}\omega_{\theta,i}^2 + I_{yy}\omega_{\eta,i}^2 + I_{zz}\omega_{\varphi,i}^2)$, the kinetic energy of the TM on the ith interval (where m_{TM} is the TM mass and I_{jj} the TM principal moment of inertia relative to the direction jj). Also the uncertainty $\sigma_{K,i}$ associated to K_i is estimated by means of the error propagation formula (see Appendix B).
- $\Delta K_i = K_{i+1} - K_i$, the variation of TM kinetic energy generated by the ith event. Also the associated uncertainty $\sigma_{\Delta K,i}$ is estimated.
- $n_{\Delta t,i}$, the number of sampling intervals over which the ith event takes place. It is computed by subtracting the final time instant of the ith interval from the initial time instant of the $i+1$-th interval, divided by the sampling time Δt.
- $e_i = \sqrt{\frac{K_{i+1}}{K_i}}$, the coefficient of restitution (COR) of the ith event, along with the associated uncertainty $\sigma_{e,i}$.
- $\mathbf{m}_i = \{m_{TM}v_{x,i}, m_{TM}v_{y,i}, m_{TM}v_{z,i}, I_{xx}\omega_{\theta,i}, I_{yy}\omega_{\eta,i}, I_{zz}\omega_{\varphi,i}\}$, the TM momentum during the ith interval. The array of associated uncertainty $\sigma_{\mathbf{m},i}$ is also estimated.
- $\|\Delta\mathbf{m}_i\| = \|\mathbf{m}_{i+1} - \mathbf{m}_i\|$, norm the variation of TM momentum generated by the ith event. The associated uncertainty $\sigma_{\|\Delta\mathbf{m}\|,i}$ is also estimated.
- $p_i = \mathbf{m}_{i+1} \cdot \mathbf{m}_i$, the scalar product of the TM momenta before and after the ith event. The associated uncertainty $\sigma_{p,i}$ is also computed.

After running the algorithm on the in-flight data, a total of approximately 1800 events (i.e., impacts or series of impacts) were found. In order to obtain useful information from those events, they are filtered on the basis of some conditions described in the following. The conditions that the ith event has to respect are:

1. The ith and $i+1$-th intervals have to be separated by at most four sampling times. This condition is introduced to limit the number of impacts taking place in the frame of the identified event (minimize the probability of considering series of impacts rather than single impacts). A graphical example is reported in Fig. 13.
2. The event has to significantly affect the TM momentum. This condition is introduced to neglect from the analysis micro impacts, i.e., impacts that do not change the TM motion direction and thus have a high β probability.

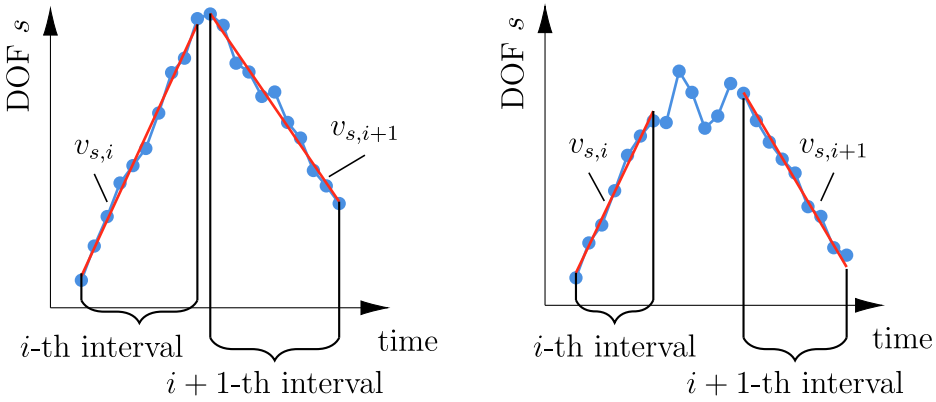

Fig. 13. Example of different events. On the left, example of a short-time event, where a limited number of impacts is present. On the right, example of a long-time event, where multiple impacts are present.

Table 5
Values of the factors used to filter the impacts found from the analysis of the in-flight data.

Factors	Value	Unit
$n_{\max}$	4	(–)
f	0.9	(–)
g_e	2.0	(–)
$g_{\|\Delta\mathbf{m}\|}$	2.0	(–)
$g_{\|p\|}$	2.0	(–)

3. The COR e_i, the momentum variation norm $\|\Delta\mathbf{m}_i\|$ and the absolute value $|p_i|$ have to be significantly larger than the associated uncertainties $\sigma_{e,i}$, $\sigma_{\|\Delta\mathbf{m}\|,i}$ and $\sigma_{p,i}$.

Those conditions are mathematically represented in Eqs. (22), (23) and (24).

$$\text{COND. 1} \quad n_{\Delta t,i} \leq n_{\max} \tag{22}$$

$$\text{COND. 2} \quad |p_i| \leq f \, \|\mathbf{m}_i\| \, \|\mathbf{m}_{i+1}\| \tag{23}$$

$$\text{COND. 3} \quad a_i \geq g_a \, \sigma_{a,i} \quad \text{where} \quad a \in \{e, \|\Delta\mathbf{m}\|, |p|\} \tag{24}$$

where the non-dimensional factors f, g_e, $g_{\|\Delta\mathbf{m}\|}$ and $g_{|p|}$ are set by the user. The factor f should be less than one to select impacts that produce a significant variation of the TM momentum. The remaining factors express the desired signal to noise ratios, i.e., the ratio between an estimated quantity and its uncertainty. In particular, the values of the g_a parameters are set according to a trade-off. On one hand, their value is large enough to guarantee that the estimated impact parameters are significantly larger than the related uncertainty; on the other hand, their value is small enough not to discard meaningful events due to an excessive filtering action.

The factors values used in the analysis are listed in Table 5

After filtering the initial data set, a total of 36 events respecting the three conditions remain. Those events are analysed in terms of their COR and of the impact line (see Section 4.1). The filtered tests are subdivided in two groups, based on the COR e being greater or lower than one. In an event where $e < 1$, the kinetic energy of the TM has been dissipated. On the contrary, if $e > 1$, the kinetic energy of the TM has been increased. Thus, is it important to distinguish the impacts on the basis of the COR value. A total of 5 events show an increase in the TM kinetic energy, and it was verified that in all of these events the TM impacted with an end-effector that was being actuated (either a release tip or a plunger being retracted). In the remaining 31 tests, characterized by $e \leq 1$, the TM impacted either a moving or a still end-effector.

4.1. Computation of the impact line

For all tests, an impact line is calculated as shown in the following. In the absence of other external forces, the relation between the contact force $\mathbf{F}_i$ and the contact torque $\mathbf{T}_i$ exerted by the ith event on the TM is expressed in Eq. (25).

$$\mathbf{r}_i(t) \times \mathbf{F}_i(t) = \mathbf{T}_i(t) \tag{25}$$

where the vector $\mathbf{r}_i$ represents the position of the contact point on the TM at the impact instant (point of application of the force $\mathbf{F}_i$). The force $\mathbf{F}_i$ and the torque $\mathbf{T}_i$ are related to the TM momentum variation by Eqs. (26) and (27).

$$\Delta\mathbf{m}_i^L = \int_0^{t^*} \mathbf{F}_i(t)\mathrm{d}t \tag{26}$$

$$\Delta\mathbf{m}_i^A = \int_0^{t^*} \mathbf{T}_i(t)\mathrm{d}t \tag{27}$$

where $\Delta\mathbf{m}_i^L$ and $\Delta\mathbf{m}_i^A$ are the linear momentum variation (superscript L) and the angular momentum variation (superscript A) of the TM (i.e., the first three and last three components of vector $\Delta\mathbf{m}_i$) and t^* represents the duration of the impact. Thus, the previous relations may be rewritten as shown in Eqs. (28) and (29).

$$\mathbf{F}_i = \Delta\mathbf{m}_i^L / t^* \tag{28}$$

$$\mathbf{T}_i = \Delta\mathbf{m}_i^A / t^* \tag{29}$$

where $\mathbf{F}_i$ and $\mathbf{T}_i$ are the integral means of the force and the torque during the impact. Combining Eqs. (28) and (29) with Eq. (25), the relation between the linear and angular TM momentum may be expressed as shown in Eq. (30).

$$\mathbf{r}_i \times \Delta\mathbf{m}_i^L = \Delta\mathbf{m}_i^A \tag{30}$$

This is algebraically equal to the linear system in Eq. (31).

$$\begin{bmatrix} 0 & m_{\mathrm{TM}}\Delta v_{x,i} & -m_{\mathrm{TM}}\Delta v_{y,i} \\ m_{\mathrm{TM}}\Delta v_{z,i} & 0 & -m_{\mathrm{TM}}\Delta v_{x,i} \\ -m_{\mathrm{TM}}\Delta v_{y,i} & -m_{\mathrm{TM}}\Delta v_{x,i} & 0 \end{bmatrix} \begin{Bmatrix} r_{x,i} \\ r_{y,i} \\ r_{z,i} \end{Bmatrix} = \begin{Bmatrix} I_{xx}\Delta\omega_{\theta,i} \\ I_{yy}\Delta\omega_{\eta,i} \\ I_{zz}\Delta\omega_{\varphi,i} \end{Bmatrix} \tag{31}$$

where $r_{x,i}$, $r_{y,i}$ and $r_{z,i}$ are the components of vector $\mathbf{r}_i$. Since the matrix on the left is singular, the space of solutions defines a line, which is called impact line. To obtain the equation of the impact line, the solution of the system can be parameterized as shown in Eq. (32).

$$\begin{Bmatrix} r_{x,i}(s) \\ r_{y,i}(s) \\ r_{z,i}(s) \end{Bmatrix} = \begin{Bmatrix} \frac{m_{\mathrm{TM}}\Delta v_{x,i}\, s - I_{yy}\Delta\omega_{\eta,i}}{m_{\mathrm{TM}}\Delta v_{z,i}} \\ \frac{m_{\mathrm{TM}}\Delta v_{y,i}\, s - I_{xx}\Delta\omega_{\theta,i}}{m_{\mathrm{TM}}\Delta v_{z,i}} \\ s \end{Bmatrix} \tag{32}$$

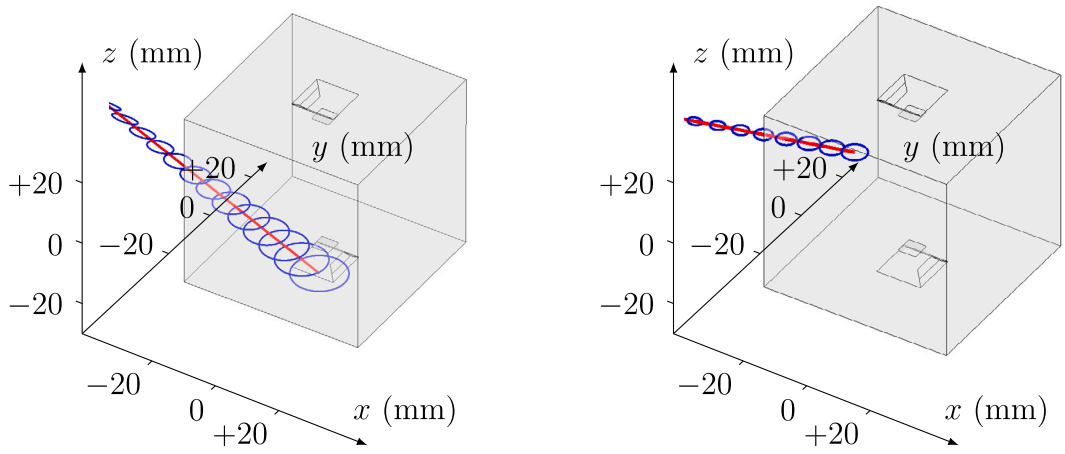

Fig. 14. Plots of the impact line (red), with 1σ uncertainty (blue ellipses). On the left the line crosses the TM indent, on the right it does not.

Uncertainties associated with $r_{x,i}(s)$ and $r_{y,i}(s)$, namely $\sigma_{r_{x,i}}(s)$ and $\sigma_{r_{y,i}}(s)$, are computed with the error propagation formula. The TMs of the LPF mission, being the sensitive bodies of the scientific measurements, have been manufactured with very tight tolerances on their geometry (10 µm maximum on 46 mm side-length) and on their homogeneity (verified with ultrasonic inspections). Therefore, the uncertainty on the TM physical parameters (mass and inertia) is neglected being much smaller that the uncertainty on the TM velocities (about 0.1% against more than 1%). The two uncertainties $\sigma_{r_{x,i}}(s)$ and $\sigma_{r_{y,i}}(s)$ are then combined to define an ellipse (Eq. (33)) that expresses the uncertainty of the position of the impact line at a given value of the coordinate s.

$$\begin{cases} x_e(s) = r_{x,i}(s) + \sigma_{r_{x,i}}(s)\cos\epsilon \\ y_e(s) = r_{y,i}(s) + \sigma_{r_{x,i}}(s)\sin\epsilon \end{cases} \tag{33}$$

where the two expressions represent the x and y coordinates of the ellipse in parametric form, with $\epsilon \in \{0, \dots, 2\pi\}$.

The impact line is plotted on the TM geometry to verify that it intersects the indent of the TM, where the impact takes place. An example is shown in Fig. 14. Of the 36 events analysed, in 13 cases (36%) the impact line does not intersects the TM close to an indent. The fact that the impact line does not cross a TM indent can be explained by the presence of multiple impacts. Indeed, it was verified from telemetry data that for each of the 13 tests the TM impacted an end-effector which was oscillating (retracted tips or repositioned plungers).

In the remaining 23 cases (64%), the impact line does intersect the TM close to an indent, i.e., the indent lays in the 2σ uncertainty envelope. In this case the TM may have undergone a single or multiple impacts (see Fig. 15). A subset of these 23 events, composed of 7 events (red dots in the graph), is of particular interest. Indeed, those are the events in which the TM impacted with non-vibrating GPRM end-effectors. In those cases the average COR is $\bar{e} = 0.62$, with a standard deviation of $\sigma_{\bar{e}} = 0.20$. This information is important, because it gives an estimation of the expected COR for a passive impact of the TM with the GPRM. In view of LISA mission, in case of a release strategy based on impacts to damp out the initial TM kinetic energy, the expected number of events n_{req} to reach a TM kinetic energy complaint with the requirements is reported in Eq. (34).

$$K_{\text{req}} = (\bar{e})^{2n_{\text{req}}} K_0 \Longrightarrow n_{\text{req}} = \frac{1}{2}\log_{\bar{e}}\left(\frac{K_{\text{req}}}{K_0}\right) \tag{34}$$

where K_0 is the initial TM kinetic energy and K_{req} is the kinetic energy computed by the maximum release velocity set by the requirements.

From Fig. 15, two additional observations are made that may be helpful in view of the LISA mission. The first is that, in case of a slow pin retraction strategy, impacts with COR greater than one taking place during the tips retraction have low probability (only one out of 10 in the graph, black dots). Indeed, this set of data has a distribution which is compatible with the 7 events where the TM impacted a non-vibrating plunger (red dots). This is verified with a Kolmogorov–Smirnov test, from which the null hypothesis at 5% confidence level is rejected.

The second observation is that, when the TM impacts a retracting plunger, the COR is more scattered and there are two events out of six (blue dots) with a COR greater than one. It is worth noticing that one of this two events has a very high COR (approximately 200). By observing the telemetry signals, it was deduced that this high COR value is caused by the TM being practically still before being hit by a plunger as soon as its retraction was commanded. Indeed, as shown in [24], the plunger trajectory is non rectilinear in the first part of its retraction, which can explain the high COR value obtained.

5. Conclusions

In this work the main objective is to characterize the impacts of a reference free falling body in space. The analysis presented is based on the telemetry data from the space mission LISA Pathfinder. Indeed, in this mission, the sensing body of the experiment is a cubic-shaped test mass released into free-fall by a dedicated mechanism. During the mission several releases were performed and almost all of them resulted in a TM state non compliant with the requirements (linear and angular velocities above the maximum values controllable by the electrostatic actuation). As a consequence, the free-falling TM impacted with the nearby end-effectors of the GPRM with velocities in the order of tens of $\mu\text{m}\,\text{s}^{-1}$ and hundreds of $\mu\text{rad}\,\text{s}^{-1}$. The telemetry data of all in-flight releases are analysed thoroughly by means of a dedicated algorithm, developed to detect the time intervals where the TM is free-falling and thus identify the impacts, or the set of impacts (named events), taking place in between. A full evaluation of the algorithm performance is presented by means of a statistical analysis. After running the algorithm with the LISA Pathfinder flight data, the identified events are analysed and some of them are filtered out based on three conditions introduced in Section 4. The remaining events are analysed on the basis of the coefficient of restitution and of the location of the impact line, described in Section 4.1. The results are coherent with the expectations. In particular, the coefficient of restitution is below one every time the TM impacts with a still end-effector. An estimation of the average COR with its uncertainty is computed averaging the events compatible with a single impact.

The estimated COR provides, for the case of study analysed, the essential information about the contribution of the impacts to the achievement of the final required state of the TM at the initialization of the following science phase, i.e., ideally zero velocity relative to

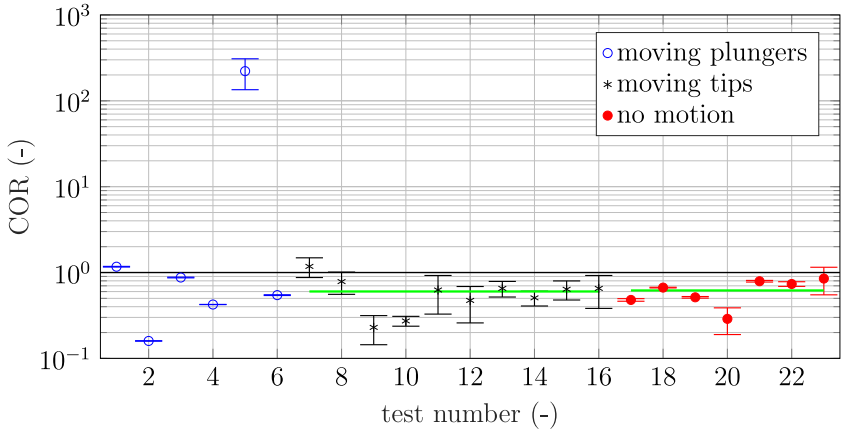

Fig. 15. Coefficient of restitution of the 23 events where the impact line intersects the TM indent. The set is divided into three subsets: plungers vibrating due to their retraction (blue), plungers vibrating due to the tips retraction (black), plungers non-vibrating (red). The green lines represent the average COR value of the last two sets.

the spacecraft. Even if this procedure was out of nominal, the analysis of the COR may be useful in the formulation and development of a possible impact-based backup release strategy for the follow-on mission, LISA, which will host a total of six TMs deployed in three spacecraft, to be released with a GPRM-like mechanism with minor modifications. Moreover, other missions in which a reference body must be mechanically released into free-fall by separating adhered surfaces may consider a similar option as a backup procedure for the achievement of the required final state.

Future developments of this work will be focused on the simulation of the TM injection into geodesic. The results of this work, in particular the average COR and the TM initial state after the release, may be used as simulation parameters for a three dimensional analysis, based either on finite element or multibody approaches. The model may include multiple modes of vibration of the plunger, to better represent the possible impact conditions, i.e., actuated tip or plunger. The simulation could be useful to estimate the dynamics of the release procedure backup strategy, in particular including the electrostatic actuation system and the control laws to be implemented to cope with the strong non-linearities produced by the impacts.

CRediT authorship contribution statement

D. Vignotto: Conceptualization, Data curation, Formal analysis, Investigation, Software, Validation, Writing – original draft, Writing – review & editing. **D. Bortoluzzi:** Conceptualization, Formal analysis, Investigation, Supervision, Writing – review & editing.

Declaration of competing interest

The authors declare that they have no conflict of interest related to the submitted paper.

Data availability

The data that has been used is confidential.

Acknowledgements

The authors wish to thank the LISA Pathfinder collaboration for the support throughout this work. This research is financially supported by ESA (European Space Agency), ASI, Italy (Italian Space Agency, under grant number 2017-29-H.1-2020), INFN, Italy (National Institute for Nuclear Physics). Moreover, the authors wish to thank the LISA Pathfinder collaboration and operations team, especially those involved in the GRS and the FEE, for technical support enabling this study.

Appendix A. Algorithms

This Appendix contains the main structure of the algorithm developed in this work, which is reported in Algorithm 1. The workflow of the two main functions of the algorithm, called *pre-release analysis* (PRA) and *reliability check* (RC) are reported in Algorithm 2 and Algorithm 3 respectively. The function PRA coincides with the sub-algorithm described in Section 3.1. The remaining part of the algorithm, including the function RC, coincides with the sub-algorithm described in Section 3.2.

Algorithm 1 Main structure

Require:
$\boldsymbol{S}$ matrix with TM DOFs as columns
$\boldsymbol{H}$ matrix of housekeeping data
$a_{\max}$ max number of intervals
$n_{\max}$ max length of an interval
κ threshold PRA function
n_{p} number of points PRA function
α threshold RC function
$\vec{\sigma}_s$ noise standard deviation array

$\{i_0, i_{\mathrm{end}}\} = \mathrm{PRA}(\boldsymbol{S}, \boldsymbol{H}, \kappa, n_{\mathrm{p}})$ ▷ Find initial and final search indexes
$i = i_0$ ▷ Initialize start index to i_0
$a = 0$ ▷ Initialize intervals counter to 0
while $a \leq a_{\max}$ and $i \leq i_{\mathrm{end}}$ **do**
  $c = 1$ ▷ Initialize flag variable to 1
  while $c = 1$ and $i \leq i_{\mathrm{end}}$ **do**
    $n = 3$ ▷ Define initial interval length
    $r = \mathrm{TRUE}$ ▷ Initialize reliability to TRUE
    while $n \leq n_{\max}$ and $r = \mathrm{TRUE}$ **do**
      $r = \mathrm{RC}(\boldsymbol{S}, i, n, \alpha, \vec{\sigma}_s)$ ▷ Check reliability of an interval
      if $r = \mathrm{FALSE}$ and $n > 3$ **then**
        $N = n - 1$ ▷ Number of points of the interval to be saved
        $c = 0$
        $i \leftarrow i - 1$ ▷ Update of the interval-start index
        EXIT WHILE CYCLE
      end if
      if r is TRUE **then**
        $n \leftarrow n + 1$ ▷ Increase interval length
      end if
    end while
    $i = i + 1$ ▷ Update of the interval-start index
  end while
  if c = 0 **then**

Save i and N
$a \leftarrow a + 1$ ▷ Update the intervals counter
$i \leftarrow i + 1$ ▷ Update of the interval-start index
end if
end while

Algorithm 2 PRA pre-release analysis function

Inputs:
$\boldsymbol{S}$ matrix with TM DOFs as columns
$\boldsymbol{H}$ matrix of housekeeping data
κ threshold
n_{p} number of point of the moving window

Outputs:
i_0 release instant
i_{end} final index for the algorithm that searches impacts

function $\{i_0, i_{\mathrm{end}}\} = \mathrm{PRA}(\boldsymbol{S}, \boldsymbol{H}, \kappa, n_p)$
$i^* \leftarrow \boldsymbol{H}$ ▷ Find last index before TM release from $\boldsymbol{H}$
$i_{\mathrm{end}} \leftarrow \boldsymbol{H}$ ▷ Find last index before electr. actuation from $\boldsymbol{H}$
for $i = 1, \dots, 6$ **do**
$\vec{s}_i = \mathrm{col}_i(\boldsymbol{S})$ ▷ Extracting the i-th TM DOF
$p_{\mathrm{int}} = \{i^* - (4 + 50), \dots, i^* - 5\}$ ▷ Def. pre-rel. interval (50 pts.)
$\bar{s} = \mathrm{mean}(\vec{s}_i(p_{\mathrm{int}}))$
$\sigma = \mathrm{std}(\vec{s}_i(p_{\mathrm{int}}))$
$j = i^* - 4$
while $j \leq i_{\mathrm{end}} - 2$ **do**
if element-wise $\vec{s}_i(j, j+1, \dots, j + n_p - 1) \geq \bar{s} + \kappa\sigma$ or
$\leq \bar{s} - \kappa\sigma$ **then**
$i_{0,i} = j$ ▷ Save the i_0 of the i-th TM DOF
EXIT WHILE CYCLE
end if
$j \leftarrow j + 1$
end while
end for
$i_0 = \min(i_{0,i})$
end function

Algorithm 3 RC reliability check function

Inputs:
$\boldsymbol{S}$ matrix having the TM DOFs as columns
i first index of the interval to be checked
n length of the interval to be checked
α value of type α probability
$\vec{\sigma}_s$ array of noise std

Output:
r reliability of an interval

function $r = \mathrm{RC}(\boldsymbol{S}, i, n, \alpha, \vec{\sigma}_s)$
$h = n - 1$
$\kappa = \sqrt{2}\mathrm{erfc}(\alpha)^{-1}$
for $j = 1, \dots, h$ **do**
$\vec{c}(j) = \frac{4 - 6j + 2h}{h - h^2}$
end for
$\vec{s}_i = \mathrm{col}_i(\boldsymbol{S})$ ▷ Extracting the i-th TM DOF
for $j = 1, \dots, 6$ **do**
$\{v_{\mathrm{fit}}, q_{\mathrm{fit}}\} = \mathrm{fit}(\vec{s}_j(i, i+1, \dots, i+h-1))$
$\hat{s} \leftarrow \mathrm{line}(v_{\mathrm{fit}}, q_{\mathrm{fit}})$ ▷ Point predicted by fitting h points
$d = |\hat{s} - \vec{s}_i(i + n - 1)|$
$t_d \leftarrow$ Noise properties ▷ Define the threshold of d
if $d \leq t_d$ **then**
$r_i = \mathrm{TRUE}$
end if
end for
if $r_i = \mathrm{TRUE}\ \forall i \in 1, \dots, 6$ **then**
$r = \mathrm{TRUE}$
else
$r = \mathrm{FALSE}$
end if
end function

Appendix B. Error propagation

Given a function $f(x_1, x_2, \dots, x_n)$, that depends on the set of physical quantities $x_1, x_2, \dots, x_n$, the uncertainty of each quantity, namely σ_i with $i \in \{1, 2, \dots, n\}$, is propagated to the function through the associated derivative. The final uncertainty is computed using the root mean square of all the propagated uncertainties [25]. This is true in the hypothesis that the uncertainties are random and independent.

$$\sigma_f = \sqrt{\sum_{n=1}^{n} \left(\frac{\partial f}{\partial x_i} \sigma_i \right)^2} \tag{35}$$

In case a subset of $x_1, x_2, \dots, x_n$ has a small uncertainty compared to other parameters, those can be neglected from the computation. For example, in the GRS case of study, the uncertainty of the mass and inertia of the TM is close to zero, thus such quantities do not play a role in the propagation of uncertainty.

References

[1] Robinson J, Nolen A. An investigation of metal matrix composites as shields for hypervelocity orbital debris impacts. Int J Impact Eng 1995;17(4):685–96, Hypervelocity Impact Proceedings of the 1994 Symposium.
[2] Lambert M, Schneider E. Hypervelocity impacts on gas filled pressure vessels. Int J Impact Eng 1997;20(6):491–8, Hypervelocity Impact.
[3] Akahoshi Y, Nakamura T, Fukushige S, Furusawa N, Kusunoki S, Machida Y, Koura T, Watanabe K, Hosoda S, Fujita T, Cho M. Influence of space debris impact on solar array under power generation. Int J Impact Eng 2008;35(12):1678–82, Hypervelocity Impact Proceedings of the 2007 Symposium.
[4] Motoyashiki Y, Hasegawa S, Okudaira K, Sato E. Micrometeoroid impact on ceramic thin components for interplanetary probe. Int J Impact Eng 2008;35(12):1666–71, Hypervelocity Impact Proceedings of the 2007 Symposium.
[5] McDonnell J. HVI phenomena: Applications to space missions. Int J Impact Eng 1999;23(1, Part 2):597–619.
[6] Schonberg WP, Ebrahim AR. Modelling oblique hypervelocity impact phenomena using elementary shock physics. Int J Impact Eng 1999;23(1, Part 2):823–34.
[7] Carrasco C, Eng D, Potocki K, Mann I. Preliminary dust-impact risk study for the "solar probe" spacecraft. Int J Impact Eng 2006;33(1):133–42, Hypervelocity Impact Proceedings of the 2005 Symposium.
[8] Williamsen J, Schonberg W, Evans H, Evans S. A comparison of NASA, DoD, and hydrocode ballistic limit predictions for spherical and non-spherical shapes versus dual- and single-wall targets, and their effects on orbital debris penetration risk. Int J Impact Eng 2008;35(12):1870–7, Hypervelocity Impact Proceedings of the 2007 Symposium.
[9] White D, Wicklein M, Clegg R, Nahme H. Multi-layer insulation material models suitable for hypervelocity impact simulations. Int J Impact Eng 2008;35(12):1853–60, Hypervelocity Impact Proceedings of the 2007 Symposium.
[10] Armano M, Audley H, Auger G, Baird JT, Bassan M, Binetruy P, Born M, Bortoluzzi D, Brandt N, Caleno M, Carbone L, Cavalleri A, Cesarini A, Ciani G, Congedo G, Cruise AM, Danzmann K, de Deus Silva M, Rosa RD, Diaz-Aguiló M, Di Fiore L, Diepholz I, Dixon G, Dolesi R, Dunbar N, Ferraioli L, Ferroni V, Fichter W, Fitzsimons ED, Flatscher R, Freschi M, García Marín AF, García Marirrodriga C, Gerndt R, Gesa L, Gibert F, Giardini D, Giusteri R, Guzmán F, Grado A, Grimani C, Grynagier A, Grzymisch J, Harrison I, Heinzel G, Hewitson M, Hollington D, Hoyland D, Hueller M, Inchauspé H, Jennrich O, Jetzer P, Johann U, Johlander B, Karnesis N, Kaune B, Korsakova N, Killow CJ, Lobo JA, Lloro I, Liu L, López-Zaragoza JP, Maarschalkerweerd R, Mance D, Martín V, Martin-Polo L, Martino J, Martin-Porqueras F, Madden S, Mateos I, McNamara PW, Mendes J, Mendes L, Monsky A, Nicolodi D, Nofrarias M, Paczkowski S, Perreur-Lloyd M, Petiteau A, Pivato P, Plagnol E, Prat P, Ragnit U, Raïs B, Ramos-Castro J, Reiche J, Robertson DI, Rozemeijer H, Rivas F, Russano G, Sanjuán J, Sarra P, Schleicher A, Shaul D, Slutsky J, Sopuerta CF, Stanga R, Steier F, Sumner T, Texier D, Thorpe JI, Trenkel C, Tröbs M, Tu HB, Vetrugno D, Vitale S, Wand V, Wanner G, Ward H, Warren C, Wass PJ,

Wealthy D, Weber WJ, Wissel L, Wittchen A, Zambotti A, Zanoni C, Ziegler T, Zweifel P. Sub-femto-g free fall for space-based gravitational wave observatories: LISA pathfinder results. Phys Rev Lett 2016;116:231101.

[11] Armano M, Audley H, Baird J, Binetruy P, Born M, Bortoluzzi D, Castelli E, Cavalleri A, Cesarini A, Cruise AM, Danzmann K, de Deus Silva M, Diepholz I, Dixon G, Dolesi R, Ferraioli L, Ferroni V, Fitzsimons ED, Freschi M, Gesa L, Gibert F, Giardini D, Giusteri R, Grimani C, Grzymisch J, Harrison I, Heinzel G, Hewitson M, Hollington D, Hoyland D, Hueller M, Inchauspé H, Jennrich O, Jetzer P, Karnesis N, Kaune B, Korsakova N, Killow CJ, Lobo JA, Lloro I, Liu L, López-Zaragoza JP, Maarschalkerweerd R, Mance D, Meshksar N, Martín V, Martin-Polo L, Martino J, Martin-Porqueras F, Mateos I, McNamara PW, Mendes J, Mendes L, Nofrarias M, Paczkowski S, Perreur-Lloyd M, Petiteau A, Pivato P, Plagnol E, Ramos-Castro J, Reiche J, Robertson DI, Rivas F, Russano G, Slutsky J, Sopuerta CF, Sumner T, Texier D, Thorpe JI, Vetrugno D, Vitale S, Wanner G, Ward H, Wass PJ, Weber WJ, Wissel L, Wittchen A, Zweifel P. Beyond the required LISA free-fall performance: new LISA pathfinder results down to 20 μHz. Phys Rev Lett 2018;120:061101.

[12] Zahnd B, Zimmermann M, Spörri R. LISA-pathfinder cage and vent mechanism development and qualification. In: 15th euro. space mechanisms & tribology symp.. ESMATS, Noordwijk; 2013.

[13] Neukom A, Romano R, Nellen PM. Testing and lessons learnt of LISA GPRM. In: 13th euro. space mechanisms & tribology symp.. ESMATS, Vienna; 2009.

[14] Bortoluzzi D, Zanoni C, Conklin J. On-ground testing of the role of adhesion in the LISA-pathfinder test mass injection phase. Adv Space Res 2017;59(10):2572–82.

[15] Bortoluzzi D, Vignotto D, Zambotti A, Armano M, Audley H, Baird J, Binetruy P, Born M, Castelli E, Cavalleri A, Cesarini A, Cruise A, Danzmann K, de Deus Silva M, Diepholz I, Dixon G, Dolesi R, Ferraioli L, Ferroni V, Fitzsimons E, Freschi M, Gesa L, Gibert F, Giardini D, Giusteri R, Grimani C, Grzymisch J, Harrison I, Hartig M-S, Heinzel G, Hewitson M, Hollington D, Hoyland D, Hueller M, Inchauspé H, Jennrich O, Jetzer P, Karnesis N, Kaune B, Korsakova N, Killow C, Lobo J, Liu L, López-Zaragoza J, Maarschalkerweerd R, Mance D, Meshksar N, Martín V, Martin-Polo L, Martino J, Martin-Porqueras F, McNamara P, Mendes J, Mendes L, Nofrarias M, Paczkowski S, Perreur-Lloyd M, Petiteau A, Pivato P, Plagnol E, Ramos-Castro J, Reiche J, Robertson D, Rivas F, Russano G, Slutsky J, Sopuerta C, Sumner T, Texier D, Thorpe J, Vetrugno D, Vitale S, Wanner G, Ward H, Wass P, Weber W, Wissel L, Wittchen A, Zweifel P, Zanoni C. In-flight testing of the injection of the LISA pathfinder test mass into a geodesic. Adv Space Res 2021;67(1):504–20.

[16] Bortoluzzi D, Vignotto D, Dalla Ricca E, Mendes J. Investigation of the in-flight anomalies of the LISA pathfinder test mass release mechanism. Adv Space Res 2021;68(6):2600–15.

[17] Tomasi M, Dalla Ricca E, Vignotto D, Bortoluzzi D. Development of a dynamical model of a release mechanism for in-flight performance prediction. Adv Space Res 2023.

[18] Weber WJ, Bortoluzzi D, Cavalleri A, Carbone L, Lio MD, Dolesi R, Fontana G, Hoyle CD, Hueller M, Vitale S. Position sensors for flight testing of LISA drag-free control. In: Saulson P, Cruise AM, editors. Gravitational-Wave Detection. 4856, International Society for Optics and Photonics, SPIE; 2003, p. 31 – 42.

[19] Gan L, Mance D, Zweifel P. LTP IS FEE sensing channel: Front-end modeling and symmetry adjustment method. IEEE Sens J - IEEE Sens J 2012;12:1071–7.

[20] Armano M, Audley H, Auger G, Baird J, Bassan M, Binetruy P, Born M, Bortoluzzi D, Brandt N, Caleno M, Cavalleri A, Cesarini A, Cruise AM, Danzmann K, de Deus Silva M, De Rosa R, Di Fiore L, Diepholz I, Dixon G, Dolesi R, Dunbar N, Ferraioli L, Ferroni V, Fitzsimons ED, Flatscher R, Freschi M, García Marirrodriga C, Gerndt R, Gesa L, Gibert F, Giardini D, Giusteri R, Grado A, Grimani C, Grzymisch J, Harrison I, Heinzel G, Hewitson M, Hollington D, Hoyland D, Hueller M, Inchauspé H, Jennrich O, Jetzer P, Johlander B, Karnesis N, Kaune B, Korsakova N, Killow CJ, Lobo JA, Lloro I, Liu L, López-Zaragoza JP, Maarschalkerweerd R, Mance D, Martín V, Martin-Polo L, Martino J, Martin-Porqueras F, Madden S, Mateos I, McNamara PW, Mendes J, Mendes L, Meshksar N, Nofrarias M, Paczkowski S, Perreur-Lloyd M, Petiteau A, Pivato P, Plagnol E, Prat P, Ragnit U, Ramos-Castro J, Reiche J, Robertson DI, Rozemeijer H, Rivas F, Russano G, Sarra P, Schleicher A, Slutsky J, Sopuerta CF, Stanga R, Sumner TJ, Texier D, Thorpe JI, Trenkel C, Tröbs M, Vetrugno D, Vitale S, Wanner G, Ward H, Wass PJ, Wealthy D, Weber WJ, Wissel L, Wittchen A, Zambotti A, Zanoni C, Ziegler T, Zweifel P, LISA Pathfinder Collaboration Collaboration Collaboration. Capacitive sensing of test mass motion with nanometer precision over millimeter-wide sensing gaps for space-borne gravitational reference sensors. Phys Rev D 2017;96:062004.

[21] Armano M, Audley H, Baird J, Born M, Bortoluzzi D, Cardines N, Castelli E, Cavalleri A, Cesarini A, Cruise AM, Danzmann K, de Deus Silva M, Dixon G, Dolesi R, Ferraioli L, Ferroni V, Fitzsimons ED, Freschi M, Gesa L, Giardini D, Gibert F, Giusteri R, Grimani C, Grzymisch J, Harrison I, Hartig M-S, Heinzel G, Hewitson M, Hollington D, Hoyland D, Hueller M, Inchauspé H, Jennrich O, Jetzer P, Karnesis N, Kaune B, Killow CJ, Korsakova N, López-Zaragoza JP, Maarschalkerweerd R, Mance D, Martín V, Martin-Polo L, Martino J, Martin-Porqueras F, Mateos I, McNamara PW, Mendes J, Mendes L, Meshksar N, Nofrarias M, Paczkowski S, Perreur-Lloyd M, Petiteau A, Pivato P, Plagnol E, Ramos-Castro J, Reiche J, Rivas F, Robertson DI, Russano G, Slutsky J, Sopuerta CF, Sumner T, Texier D, ten Pierick J, Thorpe JI, Vetrugno D, Vitale S, Wanner G, Ward H, Wass PJ, Weber WJ, Wissel L, Wittchen A, Zweifel P. Analysis of the accuracy of actuation electronics in the laser interferometer space antenna pathfinder. Rev Sci Instrum 2020;91(4):045003.

[22] Bortoluzzi D, Zanoni C, Vitale S. Improvements in the measurement of metallic adhesion dynamics. Mech Syst Signal Process 2015;52–53:600–13.

[23] Strutz T. Data fitting and uncertainty: a practical introduction to weighted least squares and beyond. Springer Vieweg Wiesbaden; 2015, p. 281.

[24] Vignotto D, Zanoni C, Tomasi M, Bortoluzzi D, Dalla Ricca E, Pretto I, Radaelli P. The role of friction in the LISA-pathfinder release mechanism anomaly. AIAA J 2023;1–10.

[25] Taylor J. Introduction to error analysis, the study of uncertainties in physical measurements. University Science Books; 1997, p. 380.